Journal of Materials Chemistry C

ROYAL SOCIETY OF CHEMISTRY

PAPER

View Article Online
View Journal | View Issue

Cite this: J. Mater. Chem. C, 2025, 13, 22315

Understanding the thermometric behaviour of $LiLuF_4:Tm^{3+},Yb^{3+}$

Mirijam Lederer,[a] Maximilian Stremel,[b] Ian Pompermayer Machado,[a] Tom Förster,[b] Syed S. Razi,[a] Markus Suta *[b] and Anna M. Kaczmarek *[a]

The Er^{3+}, Yb^{3+} upconversion couple, with its background-free green emission arising from the two thermally coupled $^2H_{11/2}$ and $^4S_{3/2}$ levels of Er^{3+}, is a classic "workhorse" example of luminescent Boltzmann thermometry. In contrast, the Tm^{3+}, Yb^{3+} couple remains far less established. The Tm^{3+}, Yb^{3+} system offers an intense $^3H_4 \rightarrow {}^3H_6$ electronic transition (800 nm) as a possible reference emission for UC thermometry in the NIR-I window. However, the Tm^{3+}, Yb^{3+} thermometry system has not yet been fully understood, limiting its potential application in medical and biological contexts, as well as in nanoelectronics, nanophotonics and in general industrial settings. In this work, we demonstrate how to exploit the temperature-dependent multiphonon relaxation from the $^3F_3$ to the $^3H_4$ level of Tm^{3+}. This relaxation is fed by energy transfer from Yb^{3+} and gives rise to two emission lines at 680 nm and 800 nm. Taking $LiLuF_4$:1% Tm, 30% Yb as a representative example, we analyzed both micro- and nanocrystalline samples to elucidate how surface-attached ligands with higher vibrational energies than the low cutoff phonon energies (~500 cm^{-1}) of the fluoride matrix itself have on the Boltzmann thermometry behaviour. We show that Tm^{3+} can only work as a wide-range Boltzmann thermometer in microcrystalline, ligand-free samples with host compounds of sufficiently low cutoff phonon energies and that its action is limited in nanocrystalline systems. A combination of experimental studies and kinetic modelling helps us to elucidate clear-cut guidelines for optimizing the performance of the Tm^{3+}, Yb^{3+} system as a luminescent thermometer and to compare this UC system to the well-established "workhorse" of the Er^{3+}, Yb^{3+} UC couple.

Received 13th May 2025,
Accepted 26th September 2025

DOI: 10.1039/d5tc01916h

rsc.li/materials-c

Introduction

Temperature sensors are in high demand, as temperature is a fundamental parameter across diverse sectors such as industry, research and medicine.[1–5] The currently used techniques to measure temperature, such as thermocouples and thermistors, are unsuitable for some catalysis applications, micro- and nanofluids, micro- and nanoelectronics, as well as biological applications, as these applications require non-invasive, remote detection.[1–4,6,7] Thermometers that do not require calibration in every media and experimental setup are advantageous for *operando* applications.[8,9] (Nano)thermometry offers outstanding properties such as fast, remote, non-invasive, accurate, sensitive and reliable temperature readouts, even for fast-moving objects in strong electromagnetic fields.[7,10–13] Utilizing trivalent lanthanides (Ln^{3+}) as emissive ions for (nano)thermometry offers stable, narrow-band emissions that cover the whole electromagnetic spectrum over wide temperature ranges.[1,4,11,12] However, the energy levels of Ln^{3+} ions are very complex ladder-like structures that result in equally sophisticated spectra, usually stemming from $4f^n$–$4f^n$ transitions. However, those $4f^n$–$4f^n$ electronic transitions are electric dipole-forbidden in centrosymmetric symmetries and only become partially allowed due to asymmetries within the crystal field surrounding the Ln^{3+} ion. This issue leads to the problem of generally weak emissions.

For some applications, it is of utmost importance to choose lanthanoid ions that exhibit bright emission lines in the biological window (BW) I (750 nm to 950 nm).[1,14–21] In this region of the electromagnetic spectrum, the overtone vibrations of *X*–H (*X* = C, N, O) groups from, for example, water or lipids, still exhibit strong absorption and can therefore potentially quench the lanthanide-based luminescence.[10,22,23] This is important as only the induced electric dipolar nature of the $4f^n$–$4f^n$ electronic transitions and the connected low absorption cross sections generally lower the overall brightness of the photoluminescence of trivalent lanthanoid ions. A common beneficial approach for luminescent thermometry is the usage

[a] NanoSensing Group, Department of Chemistry, Ghent University, Krijgslaan 289-S3, 9000 Ghent, Belgium. E-mail: anna.kaczmarek@ugent.be
[b] Inorganic Photoactive Materials, Institute of Inorganic Chemistry, Heinrich Heine University Düsseldorf, Universitätsstraße 1, 40225 Düsseldorf, Germany. E-mail: markus.suta@hhu.de

of an energy-transfer couple for upconversion (UC).[4,24,25] In this approach, a strongly absorbing sensitizer like Yb^{3+} is directly excited and subsequently transfers its energy to the activator, *e.g.*, Er^{3+} or Tm^{3+}. Moreover, the comparably large absorption cross-section of Yb^{3+} compared to the other trivalent lanthanoid ions offers the additional benefit of excitation in the NIR I window, which is relatively cheap to achieve. Moreover, NIR-excited UC emission is typically background-free, which limits the potential for systematic errors to arise in the calibration procedure of a luminescent thermometer. UC itself is beneficial as it is considered relatively background-free and therefore results in improved accuracy in luminescence thermometry.[10,26,27] A particularly popular and simple approach in UC thermometry with Ln^{3+} ions is ratiometric thermometry.[1,4,10,12] Here, the intensities of two radiative transitions are compared to each other as the intensity ratio changes with temperature. The parameter of that ratio is commonly referred to as the luminescent intensity ratio (LIR) or delta (Δ).[10,28] For a single-ion narrow-line emitter such as Er^{3+} with two thermally coupled radiatively decaying excited levels, the LIR should follow Boltzmann's law.[3,4,16,27,29]

For all kinds of applications, a high chemical, mechanical and thermal stability is important. For UC with trivalent lanthanoid ions, a low phonon energy is favorable to limit nonradiative relaxation pathways, as dictated by the energy gap law, that would otherwise lower the total decay times of the excited $4f^n$ levels.[10,30,31] $LiLuF_4$ is an excellent choice as a host material, as it has a low cutoff phonon energy ($\sim 550\ cm^{-1}$),[32,33] but it is also known to be stable for high-temperature thermometry.[30,34] It is also notable, especially in UC systems, that $LiLuF_4$ has shown high absolute UC quantum yields (QY) exceeding 5%.[35] Additionally, $LiLuF_4$ nanocrystals (NCs) can be easily synthesized with high degrees of crystallinity and high reproducibility *via* a thermal decomposition route, leading to different morphologies, including core–shell structures, by means of co-precipitation and thermal decomposition.[30,33,34]

In this work, we build upon the success of the Er^{3+}, Yb^{3+} upconversion system to investigate the potential of the Tm^{3+}, Yb^{3+} upconversion couple as an alternative luminescent thermometry system. This couple is particularly interesting because it enables the use of both blue and NIR emission through cooperative energy-transfer upconversion *via* the Yb^{3+} ions in fluorides. This is in contrast to Er^{3+}, Tm^{3+} with its $4f^{12}$ configuration that only has a limited number of spin–orbit levels, which are often energetically isolated according to the Dieke–Crosswhite diagram.[36] Accordingly, classic Boltzmann thermometry exploiting ΔE energy gaps on the order of the desired thermal energy k_BT to be probed is not straightforward with this emitter.[9,29] Generally, Tm^{3+}, Yb^{3+} systems are well-suited candidates for UC thermometry, as they offer bright emissions in the visible and NIR range.[15,37–41] To date, not much work has been devoted to the underlying mechanism of thermal coupling between excited levels of Tm^{3+}.[4,7,12,14,42] The intensity ratio of the $^3F_{2,3} \rightarrow {}^3H_6$-based emission at 680 nm and the $^3H_4 \rightarrow {}^3H_6$-based emission at 800 nm of the Tm^{3+}, Yb^{3+} system could be potentially considered thermally coupled, as the respective excited energy levels are separated by a ΔE of around 1800 cm^{-1}.[9,43] In this work, however, we demonstrate the difficulties in using this simplistic approach in the case of nanocrystalline fluorides with surface-attached ligands and their connected higher energetic vibrational modes.[29] To date, publications on the Tm^{3+}, Yb^{3+} UC system in both Na^+- and Li^+-containing fluoride-based host compounds (in micro- and nanocrystalline samples) have rarely considered the mechanism of this luminescence system, yet this knowledge plays an important role for applied thermometry.[9,29,44–46] In this work, we propose temperature-activated cross-relaxation and the consequent quenching of the emission intensity, as well as nonradiative deactivation, as mechanisms that are likely prominent in the Tm^{3+}, Yb^{3+} system. We present a theoretically motivated explanation based on $LiLuF_4$:1%Tm^{3+},30%Yb^{3+} nano- and microcrystals for ratiometric UC thermometry with this couple of lanthanoid ions. Additionally, we also investigated the influence of growing an inert $LiYF_4$ shell around the $LiLuF_4$ nanocrystalline core on its thermometric behavior. The samples were characterized by powder X-ray diffraction (PXRD), high-resolution transmission electron microscopy (HRTEM), scanning electron microscopy (SEM), fast Fourier-transform (FFT) patterns, scanning transmission electron microscopy (STEM) and energy dispersive X-ray (EDX) mapping as well as inductively coupled plasma optical emission spectroscopy (ICP-OES) to ensure that samples of high quality were obtained. Afterwards, extensive temperature-dependent steady-state and time-resolved luminescence were performed to ensure the correct modelling *via* extensive data curation. This approach guides the consequent modelling of the UC thermometry with a Tm^{3+}, Yb^{3+} system relying mainly on multiphonon relaxation not only in the discussed region of the electromagnetic spectrum but also in other regions of the electromagnetic spectrum by enabling further developments and understanding of Tm^{3+}, Yb^{3+} systems.

Experimental section

Synthesis procedure

All chemicals were obtained commercially and used without further purification unless specified otherwise. For the solid-state synthesis, saturated NH_4F was purchased from Thermo Scientific (purity: 98%$^+$) and the $LiBF_4$ was obtained from BLD Pharm (purity: 99.96%).

Synthesis of trifluoroacetate precursors for thermal decomposition synthesis

$RE(CF_3COO)_3$ with RE = Lu, Yb and Tm were prepared according to the following protocol.[30] An appropriate amount of the corresponding Ln_2O_3 was placed in a 40 mL glass vial, filled one-third with deionized (DI) water, and sonicated for 2 min in an ultrasound bath. After that, the same volume of trifluoroacetic acid was added to the mixture under a fume hood. The mixture was placed in a sand bath set at 95 °C for at least 48 h. CF_3COOLi precursors were prepared using the same method,

but LiOH was used instead of Ln_2O_3. After at least 48 h, a powder was collected.

Thermal decomposition synthesis of $LiLuF_4$:Tm,Yb core nanocrystals

The synthesis was previously reported by some of the authors of this paper[30,34] and makes use of the above-described $RE(CF_3COO)_3$ precursors dissolved in high-boiling-point solvents. 6 mL of oleic acid, 2 mL of 1-octadecene, 2 mL of oleylamine, 1 mmol CF_3COOLi, and 1 mmol of $RE(CF_3COO)_3$ (where *RE* = Tm, Yb, and Lu in appropriate amounts) were added to a three-neck glass flask. First, the mixture was heated to 120 °C under vacuum and maintained at this temperature for 30 min. After this initial step, the atmosphere was changed to a N_2 gas flow, and the mixture was stirred at 120 °C for 30 min. Finally, the mixture was heated to 320 °C under nitrogen for 40 min and then cooled to room temperature. The resulting nanocrystals were washed three times with acetone after redispersing them in cyclohexane and collected by centrifugation.

Co-precipitation synthesis of an inert $LiYF_4$ shell around $LiLuF_4$:Tm,Yb core nanocrystals

The synthesis of the undoped $LiYF_4$ inorganic shell around the doped $LiLuF_4$:Tm^{3+},Yb^{3+} core nanocrystals was also described in a previous work of some of the authors of this paper.[34] 5 mL of oleic acid, 5 mL of 1-octadecene and 1 mmol of YCl_3 were mixed in a three-neck flask. This mixture was placed under vacuum at 120 °C for 2 h until the chlorides were fully dissolved. After that, the mixture was cooled to 50 °C and the already prepared $LiLuF_4$:Tm^{3+},Yb^{3+} core nanocrystals, dispersed in 5 mL of cyclohexane, were injected into the reaction. After that, the cyclohexane was evaporated under vacuum at 120 °C for 30 min. During the evaporation step, 2 mmol of NH_4F and 1.5 mmol of LiOH were weighed off and separately dissolved in 2–3 mL of methanol in an ultrasound bath for at least 30 min. Afterwards, the mixture was cooled to 50 °C under a nitrogen flow. The dissolved NH_4F and LiOH were quickly mixed together and injected into the three-neck flask. For the necessary nucleation step, the flask was maintained at 120 °C for 30 min, after which the 5 mL of methanol was evaporated at 120 °C for 30 min under vacuum. Next, the mixture was heated to 320 °C under nitrogen and was kept there for 1 h. Lastly, the reaction was cooled to room temperature. To purify the nanocrystals, they were washed and precipitated with cyclohexane and acetone, as already described above.

Oleate ligand removal from the nanocrystals

The oleate-capped core and core–shell nanocrystals were dispersed in 5 mL of cyclohexane and mixed with 10 mL of DI water. Afterwards, 0.1 molar HCl was added to maintain the pH at 4. This mixture was sonicated for 1 h. In that process, the carboxylate groups of the oleate ligand were protonated, and the oleic acid was consequently separated from the nanocrystals in the two phases of the reaction. The now uncapped nanocrystals were precipitated in ethanol, centrifuged and then washed two times with DI water. Afterwards, the samples were dried at 80 °C overnight.

Autoclave synthesis of $LiLuF_4$:Tm,Yb microcrystals

The synthesis of the $LiLuF_4$ microcrystals was inspired by the work of Zheng *et al.*[47] For that, 1 mol of $Ln(NO_3)_3$ (where Ln = Tm, Yb, and Lu) in an appropriate ratio was mixed with 2 mL of DI water in an ultrasound bath until fully dissolved. Afterwards, 0.05 mol of EDTA was mixed with 40 mL of DI water in a round-bottomed flask, and the dissolved nitrate salts were added. The mixture was vigorously stirred for 60 min after which 1 mol of NH_4F dissolved in 12 mL of DI water and 1 mol of LiF dissolved in 8 mL of DI water were added. After continuous stirring for 20 min, the mixture was transferred to a Teflon-lined autoclave. The autoclave was placed in an oven and heated to 180 °C for 24 h after which it was cooled down naturally, and the product was collected with DI water. Subsequent steps were one to two washing steps with ethanol, after which the microcrystals were dried at 60 °C.

Solid-state synthesis of $LiLuF_4$:Tm,Yb microcrystals

$LiLuF_4$:1%Tm^{3+},30%Yb^{3+} microcrystals were prepared *via* a solid-state synthesis by dissolving the respective Ln_2O_3 oxides in concentrated hydrochloric acid in stoichiometric amounts. The solvent of the thus-obtained transparent solution was evaporated. The resulting residue was re-dissolved in DI water. Upon addition of a saturated NH_4F solution, a colourless precipitate could be isolated, dried at 80 °C overnight, and decomposed at 375 °C under a constant N_2 flow for 5 h to yield the pure rare earth fluorides. The resulting mixture was first heated at 120 °C, re-mixed with excess NH_5F_2 and re-heated at 400 °C overnight. Finally, the powder was treated with $LiBF_4$ at 500 °C for 12 h over a bed of NH_5F_2.

Characterization techniques

Transmission electron microscopy (TEM) images were obtained with a JEOL JEM-2200FS TEM, operated at 200 kV equipped with a Cs corrector. Scanning TEM (STEM) images were obtained with the same instrument utilizing the high-angle annular dark field (HAADF) and bright field (BF) detector. STEM EDX mapping was performed *via* energy dispersive X-ray (EDX) spectroscopy in HAADF-STEM mode. All TEM samples were prepared on a 300-mesh holey carbon copper grid. The nanocrystals were applied *via* placing one or two drops of a DI water suspension of nanocrystals with their ligands removed on the grid and drying at room temperature afterwards on a filter paper. Particle sizes and consequently, histograms were obtained *via* the ImageJ and Origin software. The sizing was performed with at least 100 particles on overview TEM images. STEM images, EDX maps and line scans were obtained using the program Analysis Station from JEOL. The data for the line scans were smoothed in Origin *via* a 15-point Savitzky–Golay function. Powder X-Ray diffraction (PXRD) patterns were recorded with a benchtop Rigaku Miniflex Rigaku diffractometer. The patterns were recorded from angles of 2θ = 15° to 2θ = 60°. The Rietveld refinement was performed with

Topas, refining the lattice parameters freely using the Thompson-Cox-Hastings profile function.[58] The diffractogram was plotted using the OriginPro 2024 software. The material composition was determined by inductively coupled plasma optical emission spectroscopy (ICP-OES) using an iCap 7000 duo (ThermoFisher). Scanning electron microscopy (SEM) measurements were performed using an FEI Quanta 200 FSEM. Photoluminescence (PL) spectra were recorded using an Edinburgh Instruments FLS1000 UV-vis-NIR spectrofluorometer that was equipped with a Hamamatsu R928P photomultiplier tube (PMT, Hamamatsu, Shizuoka, Japan). For measurements in the NIR range, a Hamamatsu R5509–72 photomultiplier was used to detect emissions. The excitation source was a power-tunable continuous wave (CW) laser (power limit: P_{max} = 2 W, Livingston, UK) with an excitation wavelength of 975 or 690 nm. Time-resolved measurements were performed using the same equipment, using an external modulator. High-temperature PL measurements were performed in powder after ligand removal on a Linkam (Surrey, UK) THMS600 microscope stage with ±0.1 K temperature stability. The Linkam stage was placed inside the FLS1000 setup, and the spectra were recorded from 298.15 to 498.15 K in steps of 20 K. Low (77 K) to high (870 K) temperature measurements of the $LiLuF_4$:1%Tm,30%Yb NC and MC were performed using an Edinburgh Instruments FLS1000 UV-vis-NIR spectrofluorometer. The instrument was equipped with a double excitation and emission monochromator in Czerny–Turner configuration, a thermoelectrically cooled (−253 K) photomultiplier tube PMT-980 (Hamamatsu, Shizuoka, Japan), and a 975 nm CW power-tunable laser (power limit: P_{max} = 400 mW, Livingston, UK) in a Linkam stage with optical fibre bundles. To compare the measurements, the settings for each measurement (step size and dwell time) were kept equal. The excitation source and wavelength, as well as observation wavelength/peak, are specified in the respective figure captions. Thermometrically relevant data for the micro- and nanocrystals were plotted using the TeSen software, as described above.[48] The solid-state samples, modelling and calibration data were analyzed using OriginPro 2024.

Theoretical background

In Fig. 1 the proposed energy diagram for a Tm^{3+}, Yb^{3+} UC system excited to the $^2F_{5/2}$ energy level of Yb^{3+} at 975 nm is shown with the observed emission of the Tm^{3+} centered at 680 nm stemming from the $^3F_3 \rightarrow {}^3H_6$ electronic transition (red arrow) and the 800 nm emission stemming from the $^3H_4 \rightarrow {}^3H_6$ electronic transition (brown arrow). The $^3H_4 \rightarrow {}^3H_6$ electronic transition has a high intensity based on its Judd–Ofelt allowed character and the rather energetically isolated nature of the excited $^3H_4$ level limits nonradiative relaxation.[49–51] Additionally, upconversion in the Tm^{3+}–Yb^{3+} couple can be efficiently achieved by a sequential energy transfer upon excitation of two Yb^{3+} ions at 980 nm that transfer their energy to Tm^{3+}. The process is schematically depicted in Fig. 1. In the first instance, energy transfer from Yb^{3+} to Tm^{3+} leads to population of the $^3H_5$ level that may additionally nonradiatively relax to the

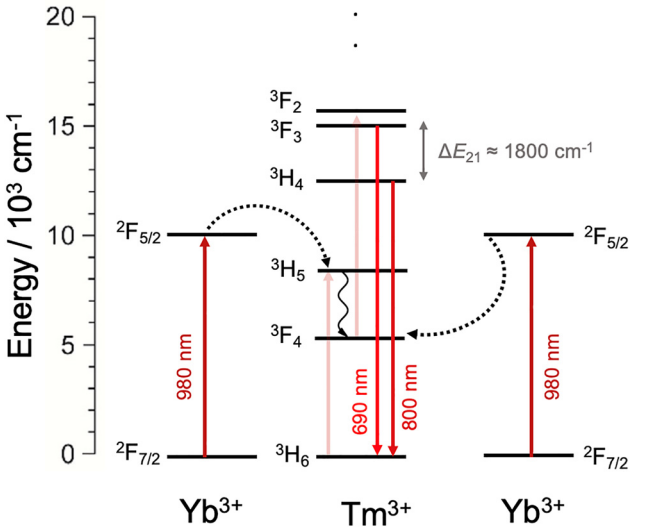

Fig. 1 Energy level diagram for the Tm^{3+}, Yb^{3+} thermometric system upon pumping Yb^{3+} at 975 nm (black arrow). Radiative transitions used for ratiometric thermometry are the $^3F_3 \rightarrow {}^3H_6$ electronic transition (680 nm emission, red arrow) and the $^3H_4 \rightarrow {}^3H_6$ electronic transition (800 nm emission, brown arrow) of Tm^{3+}. The 640 nm emission of Tm^{3+} stemming from the $^1G_4 \rightarrow {}^3F_4$ is also indicated in blue.

$^3F_4$ level. From there, energy transfer from a second excited Yb^{3+} ion ultimately leads to feeding of the $^3F_{2,3}$ levels of Tm^{3+} *via* upconversion. It is well established that both nonradiative depopulation of the $^3F_2$ electronic level and Tm^{3+}-Tm^{3+} cross-relaxation efficiently populate the $^3H_4$ electronic level, enhancing the brightness of the emission centered around 800 nm.

In principle, the $^3F_{2,3}$ and $^3H_4$ levels could be thermally coupled, enabling classic ratiometric Boltzmann thermometry using the emission lines of Tm^{3+} at 680 nm and 800 nm. However, the mutual energy gap between these two levels is around 1800 cm^{-1}, which means that nonradiative absorption (and thus, Boltzmann equilibrium) is only expected at elevated temperatures, as cutoff phonon modes ($\hbar\omega_{cut} \approx 550$ cm^{-1}) need to be thermally excited.[45] Theoretically, the $^3H_4 \rightarrow {}^3H_6$ transition is not expected to be easily thermally quenched at low temperatures, as the energy difference from the $^3H_4$ to the $^3H_5$ electronic energy level is about 4000 cm^{-1}, therefore requiring roughly 8 phonons to bridge the energy difference between these levels in $LiLuF_4$.[45] At elevated temperatures, thermal population of the low-energetic cutoff phonon modes can, however, accelerate the nonradiative relaxation process. Nevertheless, it is known that surface quenching over surface-attached ligands with X–H (X = C, N, O) groups can bridge the energy gap, even resonantly.[27,46,52,53] Thus, the thermometrically relevant energy levels $^3H_4 = |1\rangle$ and $^3F_3 = |2\rangle$ of Tm^{3+} within this work are governed by the following rate equations:

$$\dot{n}(^3F_3) = -k_{2r}n(^3F_3) - k_{nr}^{em}(T)n(^3F_3) + k_{nr}^{abs}(T)n(^3H_4) - k_{nr}^{xr}n(^3F_3) \quad (1)$$

$$\dot{n}(^3H_4) = -k_{1r}n(^3H_4) - k_{nr}^{abs}(T)n(^3H_4) + k_{nr}^{em}(T)n(^3F_3) - k_{quench}n(^3H_4) \quad (2)$$

where k_{jr} is the radiative decay rate constants of state $|j\rangle$ (j = 1, 2; see above), $k_{nr}^{abs}(T)$ and $k_{nr}^{em}(T)$ are the temperature-dependent nonradiative absorption and emission rates of the thermal coupling of the $^3H_4$ = $|1\rangle$ and $^3F_3$ = $|2\rangle$ levels of Tm^{3+}. k_{nr}^{xr} is the cross-relaxation rate additionally depopulating the $^3F_{2,3}$ levels at higher Tm^{3+} concentrations due to the energy-transfer process [Tm1, Tm2]: [$^3F_3$, $^3H_6$] → [$^3F_4$, $^3H_5$]. At the low activator fractions considered within this work (especially in the microcrystalline samples), however, cross-relaxation of the $^3F_3$ level of Tm^{3+} will only have minor relevance and may be neglected. Finally, k_{quench} denotes the rate representing any nonradiative quenching processes of the $^3H_4$ level.

Results and discussion

Nanocrystalline (NC) and microcrystalline (MC) particles with the formula $LiLuF_4$:Tm^{3+},Yb^{3+} with various ratios of Tm^{3+} and Yb^{3+}, were grown and fully characterized. HRTEM images (see Fig. 2) show nanocrystals with a homogeneous, monodisperse size distribution, as shown for example by the $LiLuF_4$:1%Tm,30%Yb NCs in the histograms in Fig. S1(a). These results were expected, as these syntheses have previously been reported by some of us in other works.[30,34] HRTEM images of the other activation ratios are shown in Fig. S2 in the SI.

SEM images of the respective $LiLuF_4$:Tm^{3+},Yb^{3+} MCs: (a and e) 1% Tm^{3+}, 30% Yb^{3+}; (b and f) 1% Tm^{3+}, 35% Yb^{3+}; (c and g) 1.5% Tm^{3+}, 30% Yb^{3+}; and (d and h) 1.5% Tm^{3+}, 35% Yb^{3+} are depicted in the SI in Fig. S3. The composition of the $LiLuF_4$:1%Tm,30%Yb core and core–shell (CS) NCs and MCs was investigated *via* ICP-OES. Their respective lanthanide activation ratios are shown in Table S1 in the SI, confirming that the synthetic and expected lanthanide percentages are in good agreement.

HRTEM images of the core–shell $LiLuF_4$:1%Tm^{3+},X%Yb^{3+}@$LiYF_4$ nanocrystals (where X = 25, 30 and 35) are shown in Fig. S4 in the SI, the histogram of the $LiLuF_4$:1%Tm^{3+},30%Yb^{3+}@$LiYF_4$ CS NCs are shown in Fig. S1(b). The increase in size after the addition of the shell is consistent with earlier findings that some of us reported for similar $LiLuF_4$@$LiYF_4$ type nanocrystals, indicating the successful formation of a shell around 2 nm in thickness over the whole surface of the core NCs.[30,34] The crystallinity of the $LiYF_4$ shell was investigated *via* FFT patterns of the HRTEM images of the $LiLuF_4$:1%Tm^{3+},30%Yb^{3+}@$LiYF_4$ nanocrystals, as shown in Fig. S5 in the SI. These patterns indicate clearly that both the core and the shell region are highly crystalline. Additionally, the integrity of the inert shell was investigated with STEM images and EDX maps with respective line scans for $LiLuF_4$:1%Tm^{3+},30%Yb^{3+}@$LiYF_4$, as presented in the SI in Fig. S6–S8. It was important to prove that no significant ion intermixing between the core and shell ions occurs and that the emissive ions in the core are properly shielded by the inert shell. As already suggested in previous works by us, ion diffusion in Li^+-containing host matrices cannot be prevented with homogeneous core–shell geometries.[34] Rather, a heterogeneous core–shell geometry with an interface such as $LiLuF_4$@$LiYF_4$ is necessary to prevent significant ion migration.

The presented core–shell nanocrystals show a regular size distribution, with an inert shell and interface region with minimal ion migration. Besides the morphology and size, the crystallinity and correct crystal phase of the materials are also of great importance, as the crystal field around the luminescent Ln^{3+} ion is essential for bright emission intensity and limited nonradiative losses.[27]

The Rietveld refinement of the PXRD patterns of the $LiLuF_4$:Tm^{3+},Yb^{3+} NCs is shown in Fig. 3: (a) 1% Tm^{3+}, 30% Yb^{3+}; (b) 1% Tm^{3+}, 35% Yb^{3+}; (c) 1.5% Tm^{3+}, 30% Yb^{3+} and (d) 1.5%Tm, 35%. The refinements are in good agreement with the 39563 ICSD reference data for $LiLuF_4$ (#PDF 00-027-1251).[54] The slight differences between the refined and detected intensities of the Bragg reflections are most likely caused by the reflection geometry of the Miniflex benchtop XRD, the related low radius of only 150 mm, and consequent texture effects based on the sample preparation. However, for determining the truly

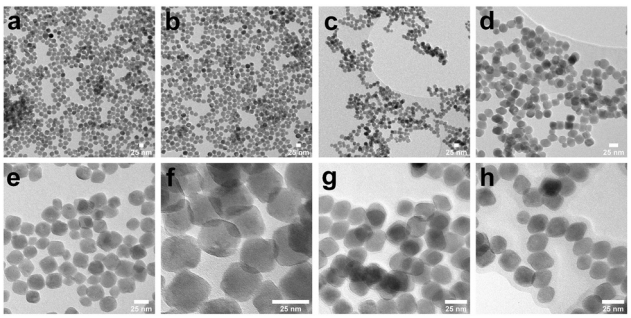

Fig. 2 TEM images of $LiLuF_4$:Tm^{3+},Yb^{3+} core nanocrystals with the following lanthanide ratios: (a and e) 1% Tm^{3+},30% Yb^{3+}; (b and f) 1% Tm^{3+}, 35% Yb^{3+}; (c and g) 1.5% Tm^{3+}, 30% Yb^{3+}; and (d and h) 1.5%Tm,35%Yb. The top images show a general overview of the nanocrystals, while the bottom images were obtained at higher magnification. The scale bar is 25 nm for all images.

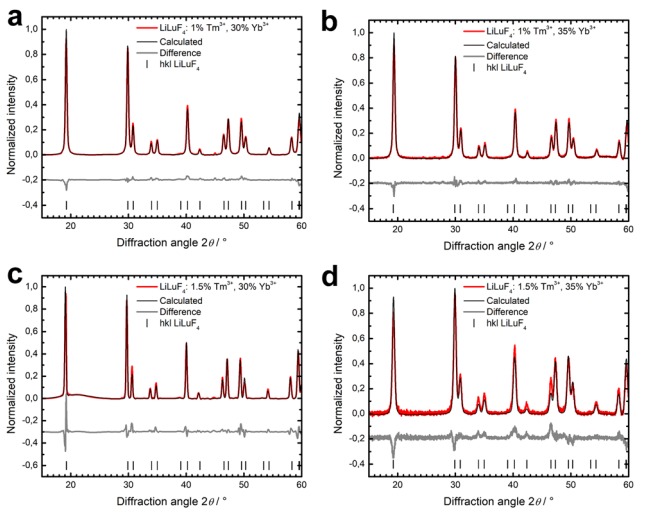

Fig. 3 Rietveld refinement of the PXRD patterns (Cu K_α radiation) of the $LiLuF_4$:Tm^{3+},Yb^{3+} NCs with different activator ratios of Tm and Yb. $LiLuF_4$ (#PDF 00-027-1251):[54] (a) 1% Tm^{3+}, 30% Yb^{3+}, (b) 1% Tm^{3+}, 35% Yb^{3+}, (c) 1.5% Tm^{3+}, 30% Yb^{3+}, and (d) 1.5% Tm^{3+}, 35% Yb^{3+}.

relevant lattice parameters, the positions of the Bragg reflections are more decisive, and the data quality is already sufficient.

The respective PXRD patterns of the NC and MC samples are depicted and discussed in the SI in Fig. S9 (NCs core), Fig. S10 (MCs) and Fig. S11 (NCs CS). These figures show that when the activation percentage of Yb^{3+} increases, the reflection position shifts to higher angles of 2θ, whereas when the amount of Tm^{3+} increases, the reflection position shifts to lower angles of 2θ. As can be deduced from Table S2, at higher doping percentages, the unit cell expands. For $LiLuF_4$:1.5%Tm^{3+},35%Yb^{3+}, the unit cell relaxes again, indicating that Tm and Yb are not incorporated into the lattice as defects anymore. For $LiLuF_4$:1%Tm^{3+},30%Yb^{3+}, it can be concluded that both Tm and Yb are not clustered in the NCs and MCs, and the unit cell expands and contracts according to the doping percentages.

Photoluminescence

The photoluminescence emission maps of the $LiLuF_4$:1%Tm,30%Yb NCs and MCs upon excitation at 975 nm are depicted in Fig. 4 (a, core NCs), (c, MCs), (e, CS NCs). The thermal response of other ratios of Tm^{3+} and Yb^{3+} in $LiLuF_4$ nano- and microcrystals is compiled in Fig. S12 (NCs) and Fig. S13 (MCs). Because the absolute intensities are prone to many experimental errors and because of the effect that this has on thermal behaviour, a given transition should instead be related to time-resolved measurements.[8,30,34,55,56] The luminescent intensity ratio $\Delta = I(680\ \text{nm})/I(800\ \text{nm})$ shows a general increase with increasing temperatures in the microcrystalline, core-only, and core–shell nanocrystals. This finding could imply thermalization between the $^3F_{2,3}$ and $^3H_4$ levels of Tm^{3+}.

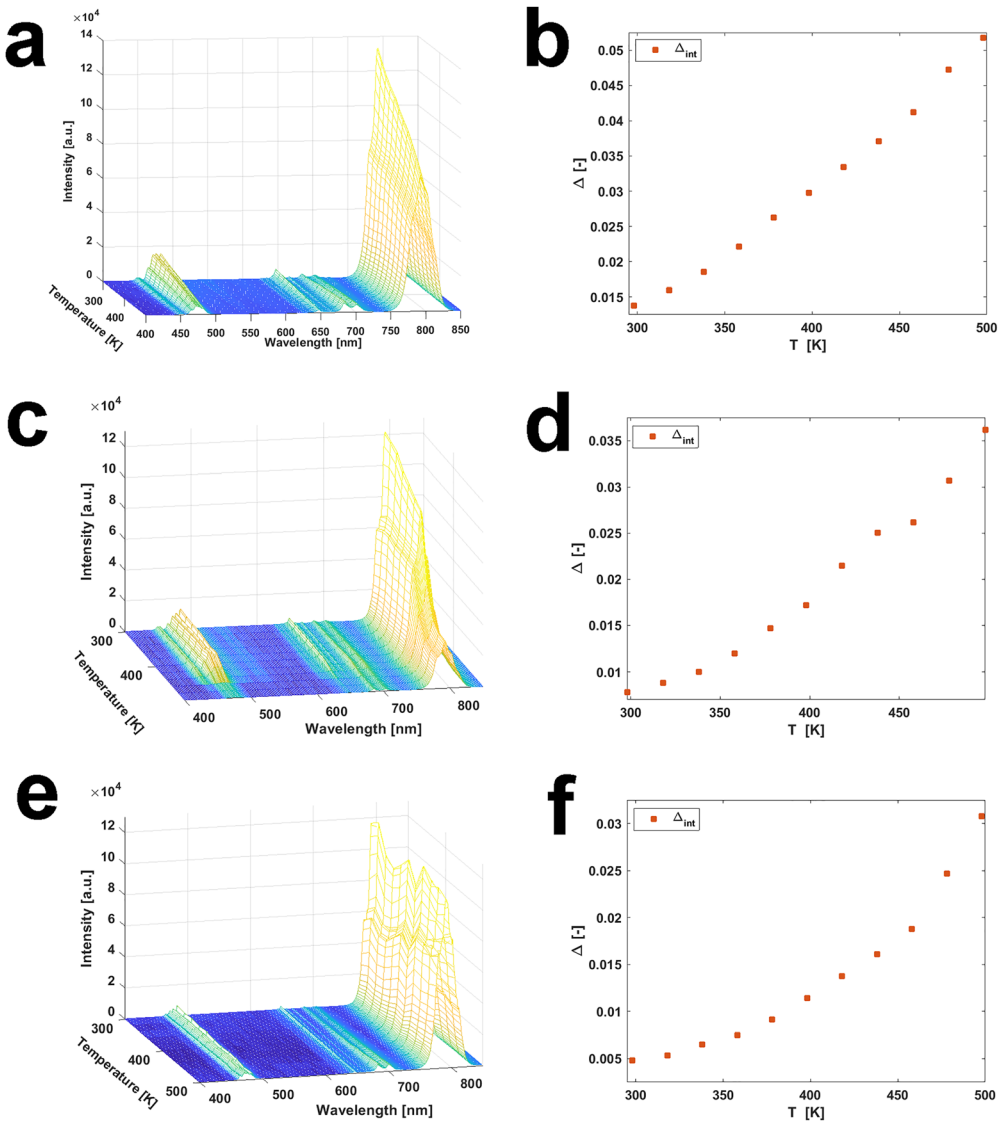

Fig. 4 Photoluminescence emission maps of $LiLuF_4$:1%Tm,30%Yb (a) core-only NCs, (c) MCs, and (e) core–shell $LiLuF_4$:1%Tm,30%Yb@$LiYF_4$ NCs excited at 975 nm in a temperature range from 298.15 to 498.15 K. The respective luminescent intensity ratio Δ (b, d and f) was calculated using the ratio of the area under the peak of the $^3F_{2,3} \rightarrow {}^3H_6$ electronic transition (emission at 680 nm) and that of the $^3H_4 \rightarrow {}^3H_6$ electronic transition (emission at 800 nm) of Tm^{3+}. Data for the other ratios of core and core–shell nanocrystals and microcrystalline samples are shown in the SI.

Attempts to fit the data to Boltzmann-type behaviour in the temperature range between 300 K and 500 K were not successful and severely underestimated the expected mutual energy gap of ΔE = 1700 cm^{-1} between the $^3F_{2,3}$ and $^3H_4$ levels. Consequently, it must be concluded that thermal equilibrium is not sustained within that temperature range for the activated core and CS NCs and MCs.

For a better understanding of the excited-state dynamics and the potential impact of cross-relaxation, time-resolved luminescence decay curves of the $^3H_4 \rightarrow {}^3H_6$-based emission of the core NCs were acquired at room temperature (see Fig. 5(a) to (c)). The results for selected samples are summarized in Table S3 in the SI. Other activation ratios are shown in Fig. S14 and summarized in Table S4. In all cases, the Yb^{3+} ions were excited at 975 nm, resulting in an initial rise component in the luminescence decay traces. In addition, a higher Tm^{3+} content in the core-only NCs results in a general decrease of the average decay time above 1 mol%, which suggests an alternative quenching pathway for the $^3H_4$ level in the $LiLuF_4$:Tm^{3+},Yb^{3+} NCs. Multiphonon relaxation can be a strong quenching mechanism for a NIR emitter such as Tm^{3+}. For example, the $^3H_4$–$^3F_4$ energy gap of around 6800 cm^{-1} can be resonantly bridged by two O–H stretching vibrational modes, while the $^3H_4$–$^3H_5$ energy gap of around 4200 cm^{-1} may be resonantly bridged by energy transfer to a C–H stretching (*ca.* 2800 cm^{-1}) and bending (*ca.* 1400 cm^{-1}) vibration. To investigate this possibility, FTIR measurements were performed. The respective FTIR spectra are shown in Fig. S15. FTIR spectra indicate the presence of the discussed organic groups on the surface for both the nano- and microcrystalline samples, even after ligand removal.

To investigate the concentration-dependent Tm^{3+}–Tm^{3+} cross-relaxation rates and thermalization dynamics, additional time-resolved luminescence decay curves of the $^3F_{2,3} \rightarrow {}^3H_6$-based emission of the core NCs were acquired at room temperature. In Fig. S16a these decays curves are presented and the respective values are given in Table S5. All curves were fitted to biexponential decay models, but despite the high quality of the fitting (R^2 = 0.99), there are deviations between the experimental data points and the fitted curves, especially at longer times, indicating a more complex deactivation pathway for the $^3F_3$ level. Nonetheless, by only varying the Tm^{3+} concentration from 0.5 to 2.0%, a clear decrease in the calculated average lifetimes is detectable (Table S5), which is a strong indicator that Tm–Tm cross relaxation is a significant quenching pathway. To verify if this is a feature of the NC systems or not, $^3F_{2,3} \rightarrow {}^3H_6$ decay curves were also measured for the $LiLuF_4$:1%Tm^{3+}, 30%Yb^{3+} solid-state sample (Fig. S16b). At the same 1% Tm^{3+}, 30% Yb^{3+} nominal activator concentrations, the NC and microcrystalline solid-state materials exhibit the same decay profile, further evidencing that Tm–Tm cross relaxation is an intrinsic deactivation pathway for the $^3F_{2,3}$ levels in $LiLuF_4$:Tm^{3+},Yb^{3+} systems, regardless of the particle size.

Thus, while the $^3F_3$ level can be effectively depopulated by cross-relaxation at higher Tm^{3+} content (both in the NCs and MCs), the $^3H_4$ level can be efficiently depopulated by multiphonon relaxation due to the high vibrational energies of the functional groups of the surface-attached ligands in nanocrystalline $LiLuF_4$. This quenching pathway apparently becomes more probable at higher Tm^{3+} contents due to an expectedly higher probability of locating Tm^{3+} ions in the vicinity of the

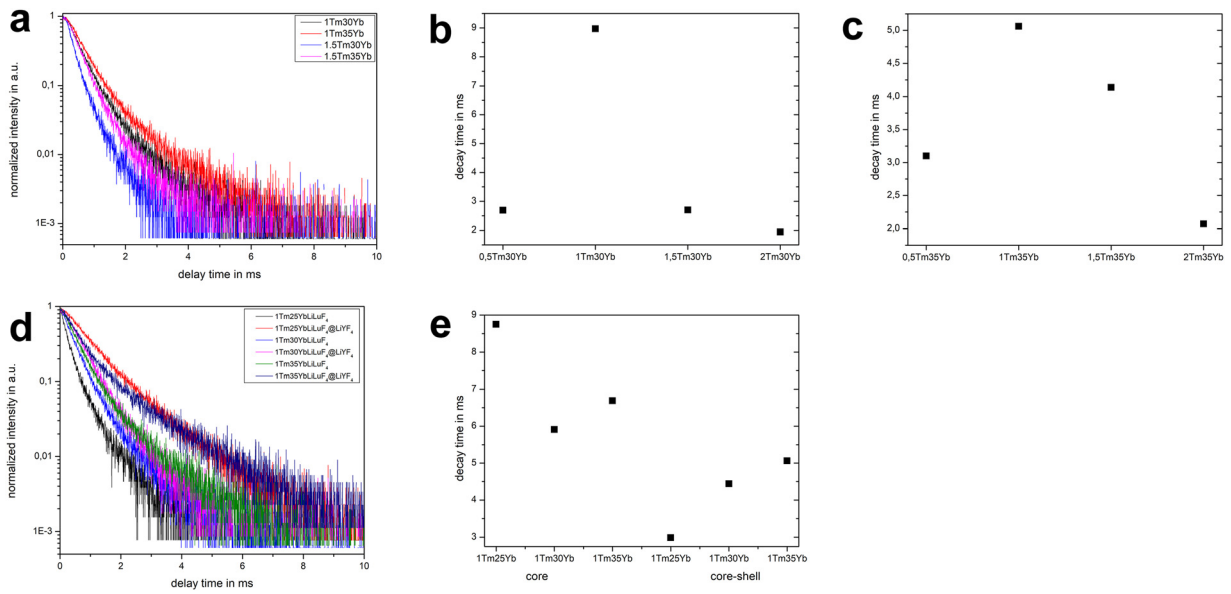

Fig. 5 Normalized luminescence decay curves of the $^3H_4 \rightarrow {}^3H_6$-based emission ($\lambda_{em}$ = 800 nm) in $LiLuF_4$ Tm,Yb nanocrystals (λ_{ex} = 975 nm, T = 298.15 K). (a) Time-resolved luminescence of the core-only $LiLuF_4$:*X*%Tm,*Y*%Yb NCs where X = 1, 1.5 and Y = 30, 35. (b) The compiled decay times for the NCs with 30% Yb. (c) the compiled decay times for the 35% Yb NC. (d) The decay curves for the $LiLuF_4$:Tm,Yb(@$LiYF_4$) core and core–shell NCs, excited at 975 nm at room temperature (298.15 K), observed at 800 nm ($^3H_4 \rightarrow {}^3H_6$ electronic transition of Tm). The curves are normalized to the respective maximum value. (e) The respective decay times and trends for the core and core–shell NCs. The respective decay curves are shown in the SI (Fig. S14).

surface of the NCs. The overall impact on the luminescent intensity ratio will thus depend on the mutual interplay of these two depopulation pathways. Crucially, both quenching mechanisms consequently pose a general limitation to using Tm^{3+} as a candidate for ratiometric thermometry as they diminish the overall achievable brightness[10,22] and thus, the signal-to-noise ratio of the two relevant emission lines at around 680 nm ($^3F_3 \rightarrow {}^3H_6$) and 800 nm ($^3H_4 \rightarrow {}^3H_6$). The proposed additional quenching pathways (cross-relaxation and multiphonon relaxation) also allow us to explain the qualitative differences between the detected delta parameter (Δ) in nano- and microcrystalline $LiLuF_4$:1%Tm,30%Yb (see Fig. 4(b) and (d)). As ligand-induced quenching depopulates the lower energy $^3H_4$ level in the nanocrystalline systems efficiently, the overall $\Delta = I_{680}/I_{800}$ ratio becomes larger compared to that of a microcrystalline sample, in which merely the lower energetic cutoff phonon modes of $LiLuF_4$ ($\approx$ 550 cm^{-1})[30] are relevant. In the core–shell NCs (see Fig. 5(e) to (f)), the situation is comparable to the MC system. In addition, cross-relaxation of the $^3F_3$ level becomes an alternative critical quenching pathway at higher Tm^{3+} contents, which is concentration-dependent.

In all three considered cases (core-only NCs, MCs and CS NCs), these two quenching mechanisms have a critical consequence for thermalization between the $^3F_3$ and $^3H_4$ levels. We will first consider the case of quenching of the $^3H_4$ level. The rate-determining step for thermalization among these two excited levels is the nonradiative absorption connected to the rate $k_{nr}^{abs}(T)$, which competes with any decay pathway of the energetically lower $^3H_4$ level. Thus, if the total decay of the $^3H_4$ level is accelerated by additional multiphonon relaxation, the kinetically determined onset temperature, T_{on}, for Boltzmann thermalization between the excited states of Tm^{3+} increases even more. This is an expected fate in core-only nanocrystalline hosts with surface-attached ligands bearing functional groups with high vibrational energies. The other scenario of cross-relaxation quenching of the higher energy $^3F_3$ level to the $^3F_4$ level generally depopulates the two relevant excited levels with no chance of phonon-assisted repopulation (ΔE $^3F_4$–$^3H_4$ = 7000 cm^{-1}). This fate is expected to be rate-determining in core–shell nanocrystalline hosts, in which multiphonon relaxation related to the presence of the surface-attached ligands can be limited.

Overall, both quenching pathways for the excited $^3F_3$ and $^3H_4$ levels of Tm^{3+} pose severe limitations for the application of this lanthanide ion as a ratiometric (Boltzmann) UC nanothermometer, and even more specifically for the often targeted physiological temperature range (25–50 °C). Only in microcrystalline samples, where the Tm^{3+} content is sufficiently low (to avoid any cross-relaxation effect), can UC ratiometric Boltzmann thermometry be applied above 540 K using the two Tm^{3+} emission lines at 680 nm ($^3F_3 \rightarrow {}^3H_6$) and 800 nm ($^3H_4 \rightarrow {}^3H_6$). Because of the previously mentioned reasons, we investigated an additional microcrystalline sample of $LiLuF_4$:1%Tm,30%Yb, prepared in a solid-state reaction, over a wide temperature range as a proof-of-concept.

This synthesis route was selected as no ligands are used in the synthesis and therefore, their consequent influence could be completely avoided. In the autoclave reaction, ligands can still be found on the particle surfaces. As can be concluded from the FTIR spectra (Fig. S15), the solid-state microcrystalline sample is completely ligand-free.

The PL results are shown in Fig. S17 and S18. As expected, Boltzmann-type behaviour is observed above $\sim$400 K, indicating that the previously mentioned competing quenching pathways were successfully suppressed by the complete removal of surface ligands. Thus, the two excited $^3F_3$ and $^3H_4$ levels, and their mutual energy gap of $\Delta E_{21} \approx 1850\ cm^{-1}$, can be employed for high-temperature thermometry in the optimum temperature range, as described in eqn (3).[27]

$$T_{opt} \in \left[\frac{\Delta E_{21}}{(2+\sqrt{2})k_B}, \frac{\Delta E_{21}}{2k_B}\right] = [758\ K,\ 1294\ K] \quad (3)$$

Conversely, a fluoride host with a maximum cutoff phonon energy of around 500 cm^{-1} would not be advisable in this case as more than 3 cutoff phonon modes are required to bridge that large energy gap, which slows down the intrinsic nonradiative coupling strength $k_{nr}(0)$ of these two excited levels ($^3F_3$ and $^3H_4$) by means of the energy gap law.[57] It has been demonstrated that the most advisable number of phonon modes is either 1 or 2, if the intrinsic coupling is sufficiently strong, such as in the case of Er^{3+}.[27,31] The reduced matrix elements for induced electric dipolar transitions, $\langle||U^{(k)}||\rangle^2$ (k = 2, 4, 6) for the electronic $^3F_3 \leftrightarrow {}^3H_4$ transition according to Carnall are $\langle||U^{(2)}||\rangle^2 = 0.0817$, $\langle||U^{(4)}||\rangle^2 = 0.3522$, and $\langle||U^{(6)}||\rangle^2 = 0.2844$ implying that this transition has an induced electric dipolar character.[36] The most critical competitive pathway to be avoided is multiphonon relaxation of the $^3H_4$ level.[36] Thus, aluminate garnet or vanadate ($\hbar\omega_{cut}$ = 800 – 900 cm^{-1}) hosts could be considered suitable alternatives for Tm^{3+} when exploiting the two indicated excited levels for ratiometric Boltzmann thermometry. Given a decay time of the $^3H_4$ level in the microcrystalline sample of around 1 ms, the expected onset temperature for Boltzmann behavior can be determined from eqn (4).[27,58]

$$T_{on} = \frac{\Delta E_{21}}{pk_B \ln\left[1 + \left(\frac{g_2 k_{nr}(0)}{k_{1r}}\right)^{1/p}\right]} \quad (4)$$

here, p is the number of phonons involved (here: p = 3–4), k_B is the Boltzmann constant, and $k_{nr}(0)$ is the intrinsic nonradiative coupling strength between the $^3F_3$ and $^3H_4$ level. The radiative decay rate of the $^3H_4$ level k_{1r} can be approximated as 1 ms^{-1}, as shown in Fig. S18(b). With the observation of $T_{on} \approx (400 \pm 10)$ K, an intrinsic nonradiative coupling strength of $k_{nr}(0) = (34.6 \pm 0.5)\ ms^{-1}$ is roughly estimated. Such a low value would be expected for thermalization involving three phonons. This clearly illustrates why Er^{3+} in β-$NaYF_4$, with a correspondingly faster intrinsic coupling strength between its green-emitting $^2H_{11/2}$ and $^4S_{3/2}$ levels of $k_{nr}(0) \approx 2\ \mu s^{-1}$ offers a much wider dynamic working range in upconversion nanocrystals.[31] Thus, even if the high energy gap of Tm^{3+} would, in principle, promise higher relative sensitivities in ratiometric luminescent thermometry, the large number of required phonons, the liability of the $^3H_4$ level towards nonradiative relaxation and the

effective optimum performance range much above physiological conditions (see eqn (3)) make Tm^{3+} unsuitable for physiological temperature sensing in this approach. Another more general issue is the spectral range around 800 nm, which is difficult to access with high accuracy for photodetectors. Finally, the ratio $g_1k_{nr}(0)/k_{2r} \approx 183$ makes the Judd–Ofelt allowed $^3H_4 \rightarrow {}^3H_6$-based emission (800 nm) much more intense compared to the $^3F_3 \rightarrow {}^3H_6$-based emission (680 nm). This clearly affects the overall expected precision of such a conceptual ratiometric thermometer, which ideally works with a $\Delta \approx 1$.[10] To investigate the influence of the surface better, different $LiLuF_4$:1%Tm^{3+},X%Yb^{3+}@$LiYF_4$ core–shell NCs where X = 25, 30, and 35 were prepared and compared to their core counterparts. The photoluminescent emission maps and corresponding Δ values are shown in Fig. 4(e) and (f) for 1% Tm^{3+}, 30% Yb^{3+} and in Fig. S19 for the other Tm/Yb ratios. Here, no significant quenching of the $^3H_4 \rightarrow {}^3H_6$ electronic transition (800 nm emission) or an increase in intensity of the $^3F_{2,3} \rightarrow {}^3H_6$ electronic transition (680 nm emission) can be observed. This is the expected behaviour for both transitions in terms of thermal quenching, as previously described in eqn (1) and (2).

Additionally, the general intensity was observed to be brighter than the core-only NCs. Decay curves and decay times for the respective core and core–shell NCs are shown in Fig. 5(d) and (e). The values of the decay times are also shown in Table S3 in the SI. The decay times are all the same or higher than the core NCs and MC counterparts. This indicates that the surface has a significant influence on both the nano- and microcrystalline samples, as no significant ion intermixing and consequently larger distances between the sensitizer and activator ion(s) were shown before. However, the interface region between the heterogeneous core–shell geometry is likely to induce local lattice distortions whilst the shell will shield the emissive ions in the core. Both of these factors will contribute to the different photoluminescence behaviour displayed.

To substantiate the previously explained model, the influence of back energy transfer was also investigated, as shown in Fig. S20 and Table S6. PL emission maps and decay curves and decay times of the $LiLuF_4$:1%Tm^{3+},30%Yb^{3+} MCs excited to the $^3H_4$ energy level (690 nm excitation) and observed *via* the $^2F_{5/2} \rightarrow {}^2F_{7/2}$ electronic transition of Yb^{3+}(1000 nm) are shown. These maps substantiate the previously discussed mechanisms of energy transfer, as Yb^{3+} shows the expected thermal deactivation. To exclude the possibility that the selected 30% Yb^{3+} is actually too high a concentration for the activator, and as a consequence, easy energy migration to surface quenchers takes place, the PL emission maps of $LiLuF_4$:1%Tm,20%Yb are shown in Fig. S21. Again, no Boltzmann behavior can be observed, substantiating the previously discussed results.

Conclusions

In this work, we considered the established Tm^{3+}, Yb^{3+} UC system for luminescent ratiometric thermometry by utilizing the emission lines of the $^3F_{2,3} \rightarrow {}^3H_6$ electronic transition (680 nm) and the $^3H_4 \rightarrow {}^3H_6$ electronic transition (800 nm) of Tm^{3+} and compared the performance of this system to the well-established ''workhorse'' example of the green-emitting Er^{3+}, Yb^{3+} UC system. We selected $LiLuF_4$:1%Tm,30%Yb as a representative example in this work. Both micro- and nanocrystalline samples were considered to investigate the impact of surface-attached ligands with higher vibrational energies than the low cutoff phonon energies ($\sim$550 cm^{-1}) of the fluoride host itself. While the microcrystalline samples prepared by a solid-state reaction do indeed show luminescence intensity ratios of $\Delta = I_{680\ nm}/I_{800\ nm}$ with Boltzmann behavior above 400 K and can be considered sensitive Boltzmann thermometers (S_r(450 K) = 1.32% K^{-1}), the nanocrystalline samples and microcrystalline samples with remaining surface ligands are not suitable for luminescent thermometry at those temperatures. This observation can be related to the susceptibility of the lower energy $^3H_4$ level to nonradiative multiphonon relaxation over ligands with high surface vibrational energies. In addition, the higher energy $^3F_3$ level is prone to irreversible cross-relaxation at higher Tm^{3+} activator fractions. For effective luminescent thermometry at elevated temperatures with the Tm^{3+}, Yb^{3+} UC system, we advise selecting hosts with slightly higher cutoff phonon energies such as aluminate-based garnets or vanadates ($\hbar\omega_{cut}$ = 800 – 900 cm^{-1}). Overall, however, the combination of experimental work on both micro- and nanocrystalline phosphors coupled with excited-state dynamics modelling helps substantiate that, despite the recorded success of the Tm^{3+}, Yb^{3+} couple for NIR-to-blue UC, Tm^{3+} cannot readily outperform the established lanthanoid ion Er^{3+} as a Boltzmann thermometer given the specific electronic energy level landscape of these two activators. This is of utmost importance to consider, as pushing the performance limits of the Er^{3+}–Yb^{3+} couple is still necessary for applications, and the Tm^{3+}–Yb^{3+} pair was and still is extensively discussed as an alternative. This study demonstrates, however, that classic Boltzmann thermometry with the Tm^{3+} ion is not feasible for that purpose, especially within the physiological temperature regime.

Author contributions

M. L. was responsible for investigation, writing, reviewing, editing and visualisation. M. S. was responsible for investigation and visualisation. I. P. M. was responsible for investigation. T. F. was responsible for investigation and visualisation. S. S. R. was responsible for investigation. M. S. was responsible for investigation, writing, reviewing, editing and visualisation. A. M. K. was responsible for conceptualization, funding acquisition, project administration, supervision, editing and reviewing.

Conflicts of interest

There are no conflicts to declare.

Data availability

All raw data from the respective figures presented in the manuscript have been uploaded to a repository: **https://doi.org/10.5281/zenodo.15187316**.

Supplementary information: HRTEM images, histograms, SEM images, STEM images and EDX maps, EDX line scans, PXRD patterns, FFT patterns, ICP-OES results, (high temperature) photoluminescence measurements and respective calculations, decay times, and FTIR spectra. See DOI: **https://doi.org/10.1039/d5tc01916h**.

Acknowledgements

This work is part of a project that has received funding from the European Research Council (ERC) under the European Union's Horizon 2020 research and innovation program (grant agreement No. 945945). Markus Suta is grateful for a scholarship from the "Young College" of the North-Rhine Westphalian Academy of Sciences, Humanities, and the Arts. The authors are indebted to Andries Meijerink for very helpful discussions.

Notes and references

1 M. Dramićanin, *Luminescence thermometry: Methods, materials, and applications*, Woodhead Publishing, an imprint of Elsevier, Duxford, United Kingdom, 2018.
2 *Thermometry at the Nanoscale: Techniques and Selected Applications*, ed L. D. Carlos and F. Palacio, The Royal Society of Chemistry, 2015.
3 D. Jaque Garcia and F. Vetrone, *Nanoscale*, 2012, 4301–4326.
4 M. Jia, X. Chen, R. Sun, D. Wu, X. Li, Z. Shi, G. Chen and C. Shan, *Nano Res.*, 2023, **16**, 2949–2967.
5 B. Harrington, Z. Ye, L. Signor and A. D. Pickel, *ACS Nanosci. Au*, 2024, **4**, 30–61.
6 A. M. Kaczmarek, S. Abednatanzi, D. Esquivel, C. Krishnaraj, H. S. Jena, G. Wang, K. Leus, R. Van Deun, F. J. Romero–Salguero and P. Van Der Voort, *Microporous Mesoporous Mater.*, 2020, **291**, 109687.
7 S. Premcheska, M. Lederer and A. M. Kaczmarek, *Chem. Commun.*, 2022, **58**, 4288–4307.
8 J. C. Martins, A. R. N. Bastos, R. A. S. Ferreira, X. Wang, G. Chen and L. D. Carlos, *Adv. Photo Res.*, 2021, 2000169.
9 N. Stopikowska, M. Runowski, P. Woźny, S. Goderski and S. Lis, *J. Lum.*, 2020, **228**, 117643.
10 C. D. S. Brites, R. Marin, M. Suta, A. N. Carneiro Neto, E. Ximendes, D. Jaque and L. D. Carlos, *Adv. Mater.*, 2023, **35**, 2302749.
11 C. D. S. Brites, S. Balabhadra and L. D. Carlos, *Adv. Opt. Mat.*, 2018, 1801239.
12 L. Đačanin Far and M. Dramićanin, *Nanomaterials*, 2023, **13**, 2904.
13 B. M. Walsh, in *Advances in Spectroscopy for Lasers and Sensing*, ed B. Di Bartolo and O. Forte, Springer Netherlands, Dordrecht, 2006, pp. 403–433.
14 M. Quintanilla, M. Henriksen-Lacey, C. Renero-Lecuna and L. M. Liz-Marzán, *Chem. Soc. Rev.*, 2022, **51**, 4223–4242.
15 X. Qin, J. Wang and Q. Yuan, *Front. Chem.*, 2020, **8**, 608578.
16 A. Bednarkiewicz, L. Marciniak, L. D. Carlos and D. Jaque, *Nanoscale*, 2020, **12**, 14405–14421.
17 N. Jurga, M. Runowski and T. Grzyb, *J. Mater. Chem. C*, 2024, **12**, 12218–12248.
18 H. Fu, Y. Ma, Y. Liu and M. Hong, *Chem. Commun.*, 2021, **57**, 2970–2981.
19 A. Kar and A. Patra, *Nanoscale*, 2012, **4**, 3608.
20 R. Ghosh Chaudhuri and S. Paria, *Chem. Rev.*, 2012, **112**, 2373–2433.
21 H. Rijckaert and A. M. Kaczmarek, *Chem. Commun.*, 2020, **56**, 14365–14368.
22 T. P. Van Swieten, A. Meijerink and F. T. Rabouw, *ACS Photonics*, 2022, **9**, 1366–1374.
23 N. Stopikowska, P. Woźny, M. Suta, T. Zheng, S. Lis and M. Runowski, *J. Mater. Chem. C*, 2023, **11**, 9620–9627.
24 C. Ma, X. Xu, F. Wang, Z. Zhou, D. Liu, J. Zhao, M. Guan, C. I. Lang and D. Jin, *Nano Lett.*, 2017, **17**, 2858–2864.
25 A. Ćirić, Ł. Marciniak and M. D. Dramićanin, *J. Appl. Phys*, 2022, **131**, 114501.
26 J. Zhou, B. del Rosal, D. Jaque, S. Uchiyama and D. Jin, *Nat. Methods*, 2020, **17**, 967–980.
27 M. Suta and A. Meijerink, *Adv. Theory Simul.*, 2020, **3**, 2000176.
28 A. Bednarkiewicz, J. Drabik, K. Trejgis, D. Jaque, E. Ximendes and L. Marciniak, *Appl. Phys. Rev.*, 2021, **8**, 011317.
29 M. Runowski, P. Woźny, N. Stopikowska, I. R. Martín, V. Lavín and S. Lis, *ACS Appl. Mater. Interfaces*, 2020, **12**, 43933–43941.
30 A. M. Kaczmarek, M. Suta, H. Rijckaert, T. P. van Swieten, I. Van Driessche, M. K. Kaczmarek and A. Meijerink, *J. Mater. Chem. C*, 2021, **9**, 3589–3600.
31 M. Suta, *Nanoscale*, 2025, **17**, 7091–7099.
32 Y. Zhu, S. Zhao, B. Zhou, H. Zhu and Y. Wang, *J. Phys. Chem. C*, 2017, **121**, 18909–18916.
33 J. Liu, H. Rijckaert, M. Zeng, K. Haustraete, B. Laforce, L. Vincze, I. Van Driessche, A. M. Kaczmarek and R. Van Deun, *Adv. Funct. Mater.*, 2018, **28**, 1707365.
34 M. Lederer, H. Rijckaert and A. M. Kaczmarek, *ACS Appl. Nano Mater.*, 2023, **6**, 2438–2449.
35 P. Huang, W. Zheng, S. Zhou, D. Tu, Z. Chen, H. Zhu, R. Li, E. Ma, M. Huang and X. Chen, *Angew. Chem.*, 2014, **126**, 1276–1281.
36 W. T. Carnall, H. Crosswhite and H. M. Crosswhite, *Energy level structure and transition probabilities in the spectra of the trivalent lanthanides in LaF_3, 1978.*
37 Y. Chang, H. Chen, X. Xie, Y. Wan, Q. Li, F. Wu, R. Yang, W. Wang and X. Kong, *Nat. Commun.*, 2023, **14**, 1079.
38 H.-W. Chien, C.-H. Huang, C.-H. Yang and T.-L. Wang, *Nanomaterials*, 2020, **10**, 2477.
39 N.-N. Dong, M. Pedroni, F. Piccinelli, G. Conti, A. Sbarbati, J. E. Ramírez-Hernández, L. M. Maestro, M. C. Iglesias-de la Cruz, F. Sanz-Rodriguez, A. Juarranz, F. Chen, F. Vetrone, J. A. Capobianco, J. G. Solé, M. Bettinelli, D. Jaque and A. Speghini, *ACS Nano*, 2011, **5**, 8665–8671.

40 I. N. Bazhukova, V. A. Pustovarov, A. V. Myshkina and M. V. Ulitko, *Opt. Spectrosc.*, 2020, **128**, 2050–2068.
41 B. Yang, H. Chen, Z. Zheng and G. Li, *J. Lumin.*, 2020, **223**, 117226.
42 D. Gao, Y. Liang, J. Gao, H. Xin, L. Wang, S. Yun and X. Zhang, *J. Lumin.*, 2021, **238**, 118261.
43 B. Bendel and M. Suta, *J. Mater. Chem. C*, 2022, **10**, 13805–13814.
44 M. Misiak, O. Pavlosiuk, M. Szalkowski, A. M. Kotulska, K. A. Ledwa and A. Bednarkiewicz, *Nanotechnology*, 2023, **34**, 345702.
45 D. V. Pominova, V. Y. Proydakova, I. D. Romanishkin, A. V. Ryabova, P. V. Grachev, V. I. Makarov, S. V. Kuznetsov, O. V. Uvarov, V. V. Voronov, A. D. Yapryntsev, V. K. Ivanov and V. B. Loschenov, *Laser Phys. Lett.*, 2020, 13.
46 H. Suo, P. Zhao, X. Zhang, Y. Guo, D. Guo, J. Chang, J. Chen, P. Li, Z. Wang, H. Wei, W. Zheng and F. Wang, *Nat. Commun.*, 2025, **16**, 3249.
47 Y. Zheng, H. Xu, X. Xu, L. Xu, S. Wang and S. Wu, *J. Alloys Compd.*, 2022, **910**, 164778.
48 A. M. Kaczmarek, R. Van Deun and M. K. Kaczmarek, *Sens. Actuators, B*, 2018, **273**, 696–702.
49 L. Giordano, M. Nunes, V. Teixeira and L. Rodrigues, *J. Braz. Chem. Soc.*, 2021, **32**, 1552–1558.
50 X. Zhai, P. Lei, P. Zhang, Z. Wang, S. Song, X. Xu, X. Liu, J. Feng and H. Zhang, *Biomaterials*, 2015, **65**, 115–123.
51 O. Savchuk, J. J. Carvajal Marti, C. Cascales, P. Haro-Gonzalez, F. Sanz-Rodríguez, M. Aguilo and F. Diaz, *Nanomaterials*, 2020, **10**, 993.
52 N. J. J. Johnson, S. He, S. Diao, E. M. Chan, H. Dai and A. Almutairi, *J. Am. Chem. Soc.*, 2017, **139**, 3275–3282.
53 M. Lin, Y. Zhao, S. Wang, M. Liu, Z. Duan, Y. Chen, F. Li, F. Xu and T. Lu, *Biotechnol. Adv.*, 2012, **30**, 1551–1561.
54 X. Jiang, C. Cao, W. Feng and F. Li, *J. Mater. Chem. B*, 2016, **4**, 87–95.
55 Z. Wang, J. Christiansen, D. Wezendonk, X. Xie, M. A. Van Huis and A. Meijerink, *Nanoscale*, 2019, **11**, 12188–12197.
56 S. A. Burikov, O. E. Sarmanova, A. A. Fedyanina, I. V. Plastinin and T. A. Dolenko, *Spectrochim. Acta, Part A*, 2025, **334**, 125902.
57 L. A. Riseberg and H. W. Moos, *Phys. Rev.*, 1968, **174**, 429–438.
58 T. P. Van Swieten, J. M. Steenhoff, A. Vlasblom, R. De Berg, S. P. Mattern, F. T. Rabouw, M. Suta and A. Meijerink, *Light: Sci. Appl.*, 2022, **11**, 343.